

# Signatures of UV radiation around low-mass protostars in the Serpens Main with IRAM 30m

Agnieszka Mirocha<sup>1,2</sup>, Agata Karska<sup>2</sup>, Lars E. Kristensen<sup>3</sup>, Marcin Gronowski<sup>4</sup>, Miguel Figueira<sup>5</sup>, Marcin Gładkowski<sup>2,6</sup>, Michał Żółtowski<sup>2</sup>, and Łukasz Tychoniec<sup>7</sup>

<sup>1</sup> Astronomical Observatory of the Jagiellonian University, ul. Orla 171, 30-244 Kraków, Poland  
e-mail: amirocha@doctoral.uj.edu.pl

<sup>2</sup> Centre for Astronomy, Faculty of Physics, Astronomy and Informatics, Nicolaus Copernicus University, ul. Grudziądzka 5, 87-100 Toruń, Poland

<sup>3</sup> Centre for Star and Planet Formation, Niels Bohr Institute and Natural History Museum of Denmark, University of Copenhagen, Øster Voldgade 5-7, DK-1350 Copenhagen K, Denmark

<sup>4</sup> Faculty of Physics, University of Warsaw, ul. Pasteura 5, 02-093 Warszawa, Poland

<sup>5</sup> National Centre for Nuclear Research, ul. Pasteura 7, 02-093 Warszawa, Poland

<sup>6</sup> Nicolaus Copernicus Astronomical Center, ul. Rzymska 8, 87-100 Toruń, Poland

<sup>7</sup> Leiden Observatory, Leiden University, P.O. Box 9513, NL-2300RA Leiden, The Netherlands

Received [Month] [Day], 2019; accepted [Month] [Day], 2019

## ABSTRACT

**Context.** The Serpens Main is one of the most studied star forming region containing low-mass protostars. Observations at submillimetre range allow to determine physical and chemical processes around young stellar objects.

**Aims.** We aim to characterise the UV radiation in the surroundings of the low-mass protostars. We analyse the excitation and spatial extent of HCN, CN, CS and their isotopologues to identify the underlying processes. We can investigate the feedback from protostars and the excitation mechanisms of molecules.

**Methods.** We present  $\sim 30$  arcmin<sup>2</sup> IRAM 30m maps of CN  $J = 1 - 0$ , HCN  $J = 1 - 0$ , and CS  $J = 3 - 2$  encompassing 10 Class 0/I protostars. We calculate HCN and CN column densities toward protostars and selected outflows positions. The column densities are compared with the Nahoon astrochemical model of molecules abundances in order to characterise UV radiation field.

**Results.** Emission of HCN  $J = 1 - 0$  and CS  $J = 3 - 2$  is co-spatial with outflows, whereas CN emission peaks at the positions of protostars. CN and HCN column densities are of the order of  $10^{13}$ - $10^{14}$  cm<sup>-2</sup>. Regardless of gas parameters, CN/HCN column density ratio is 1-10. This result can be reproduced by providing an additional UV radiation source of 0.001 to 0.044  $G_0$ .

**Conclusions.** The UV radiation field is significantly higher in the closest distances from protostars. The astrochemical model shows that an additional source of UV radiation is needed to cover the abundances range indicated by observations.

**Key words.** astrochemistry – stars: formation – ISM: molecules – ISM: individual objects: Serpens Main – Submillimeter: ISM

## 1. Introduction

Low-mass stars are the most numerous objects among stellar population in galaxies (Kroupa 2002). At first stages of star formation protostars are formed inside molecular cloud, surrounded by massive envelopes exceeding for  $10^4$  AU in diameter (Lada 1987; Larson 2003; Bergin & Tafalla 2007). The embedded phases of low-mass star formation (Class 0/I YSOs, Andre et al. 1993) is characterised by gas and dust accretion from an envelope and bipolar, collimated outflows which carry out molecular gas from the dense core (Zuckerman et al. 1976, Arce & Sargent 2006).

The Serpens star forming cloud is one of the most active sources containing low-mass protostars within 500 pc (Evans et al. 2009). The latest distance estimations based on astrometric observations (Ortiz-León et al. 2017) place the cloud at  $436 \pm 9$  pc away. The cloud was selected as one of the target sources in the Spitzer Space Telescope Legacy project ‘From Molecular Cores to Planet-forming Disks’ (Evans et al. 2003) and the Herschel Gould belt survey (André et al. 2010). The first survey provided embedded sources identification based on

color-color diagrams (Harvey et al. 2007) and detailed calculation of bolometric luminosities, temperatures, and envelope masses (Enoch et al. 2009), as well as the catalog of identified YSOs (Dunham et al. 2015). The second program aims to characterise luminosities, temperatures and density profiles of prestellar cores and Class 0 protostars, and determine core mass functions and protostar luminosity functions.

The cloud core (hereafter referred to as Serpens Main) has been found in far-infrared and submillimeter observations as a dense area with several deeply embedded protostars Class 0/I (Casali et al. 1993, Hurt & Barsony 1996, Testi & Sargent 1998). Molecular observations of CO rotational transitions revealed outflows connected with the protostars (Davis et al. 1999, Dionatos et al. 2010). Individual sources were probed with the Water in Star-Forming Regions with the Herschel Space Observatory (WISH) project (van Dishoeck et al. 2011) and the ‘Dust, Ice, and Gas in Time’ (Green et al. 2013).

Tracing the physical and chemical processes dominated by UV radiation lead to better understanding of the protostellar evolution. Signatures of chemical tracers characteristic

of warmer regions were noticed in the Serpens Main region (McMullin et al. 2000, Yıldız et al. 2015). The large Spitzer and Herschel surveys brought new insights into physical properties of the gas around low-mass protostars. Herschel-PACS observations of the high-J CO emission around low-mass protostars including Ser-SMM1, Ser-SMM3 and Ser-SMM4 showed the presence of a warm component about  $T_{\text{rot}} \sim 300$  K, hot component of  $T_{\text{rot}} \sim 600 - 800$  K (Karska et al. 2013, Green et al. 2013) and very hot component exceeding 1000 K for some sources (Manoj et al. 2013). The high-temperature CO emission can be explained as shocked-heated gas created by UV-irradiated shocks (Kristensen et al. 2017). Shock waves are created in the inner part of accretion disk where the gas is heated by the 10,000 K radiation field (Spaans et al. 1995). UV photons propagate in low-density outflow cavities for large distances, modifying the chemical composition of low-mass neighbourhood.

Previous studies of energetic processes around low-mass protostars showed observational premises of the influence of UV radiation on molecules. At protostars positions was observed higher emission of [C I] than in off-source positions what brought to conclusion of photodissociation CO (van Kempen et al. 2009). The fluxes of [OI] and [CII] are significantly higher than fully-shielded C-shock models (Karska et al. 2018). The other photodissociation tracer  $\text{H}_2\text{O}/\text{OH}$  showed a few order of magnitude disagreement with shock models (Karska et al. 2014). Therefore, ultraviolet radiation may play an important role in low-mass protostars surroundings.

The relative abundance of CN and HCN molecules is widely used a tracer of UV radiation in different astronomical context: reflection nebulae (e.g. Fuente et al. 1995), proto-planetary disks (e.g. Chapillon et al. 2012), proto-brown dwarfs (e.g. Riaz et al. 2018). CN is a product of photodissociation of HCN with the photodissociation rate of  $1.64 \times 10^{-9}$ . CN has smaller photodissociation rate of  $5.19 \times 10^{-10}$  (Heays et al. 2017), thus is not that sensitive for photodissociation as HCN. Since CN and HCN can be photodissociated selectively, therefore the CN/HCN ratio probes regions affected by UV radiation. The ratio is the highest near the source of the UV emission, and decreases with the distance from the source (Fuente et al. 1993). We propose to use CN and HCN molecules as a tracer of UV radiation field around low-mass protostars.

Ultraviolet radiation can propagate in large scales of 1000 AU (Kristensen et al. 2017), changing the properties of the surrounding matter. Since the UV radiation around low-mass protostars was studied only in the source position (Stäuber et al. 2007, Riaz et al. 2018) or in the source closest neighbourhood (Hogerheijde et al. 1999, Bachiller et al. 2001, Jørgensen 2004), the spatial extent of UV fields in larger scales is the matter of question. We address the following questions in: How does the UV radiation affect the chemistry of the surrounding of the low-mass? If the molecules are dissociated in the inner envelope or in the outflows? What is the spatial extent of the UV fields from protostars and their outflows? What is the typical strength of UV radiation around Class 0/I protostars?

We present the CN, HCN, CS and their isotopologues molecular data observed in the Serpens Main star forming region. Section 2 contains the overview of the observations and the targeted sample. The results derived from the observations are shown in the Section 3, while further analysis of the data in Section 4. In the section 5 we refer to the previous studies of the topic and provide the discussion of the results. The summarising Section 6 is closed with our conclusions.

## 2. Observations

### 2.1. IRAM data and reduction process

The Serpens Main star forming region was observed with IRAM 30 between 14 and 17 July 2009 (project no. xxx, PI: L. Kristensen). We used the Eight MIXer Receiver (EMIR) as the frontend. The observations were performed in the EMIR bands E090 (molecule HCN  $J = 1 - 0$ ) covering the range 73-117 GHz and E150 (molecules CN  $J = 1 - 0$  and CS  $J = 3 - 2$ ) covering the frequencies between 125 and 184 GHz. Due to the EMIR receiver wide bands additional molecular lines of  $\text{C}^{34}\text{S}$   $J = 3 - 2$ ,  $\text{H}^{13}\text{CN}$   $J = 1 - 0$  and  $\text{H}^{13}\text{CN}$   $J = 2 - 1$  were also observed. The backend was the Versatile SPectrometer Array (VESPA) autocorrelator and the 1 MHz filterbank reaching the spectral resolution of 39 kHz (E150 band) and 78 kHz (E090 band). The telescope beam size varies from  $14''$  at 172.68 GHz to  $29''$  at 86.34 GHz (Table 1). The antenna temperatures were converted to main-beam brightness temperature  $T_{\text{MB}}$  using the main beam efficiency according to the expression:  $T_{\text{MB}} = T_{\text{A}}/\eta_{\text{MB}}$ . The exact upper levels energies, line frequencies, beam sizes and beam efficiencies are given in Table 1. Observations included scans of the Ser-SMM1 (centered at  $\alpha_{\text{J2000}} = 18^{\text{h}}29^{\text{m}}49.6^{\text{s}}$ ,  $\delta_{\text{J2000}} = +01^{\circ}15'20.5''$  with  $V_{\text{LSR}} = +8.5$  km/s) and the Ser-SMM3/Ser-SMM4 (centered at  $\alpha_{\text{J2000}} = 18^{\text{h}}29^{\text{m}}56.6^{\text{s}}$ ,  $\delta_{\text{J2000}} = +01^{\circ}14'00.3''$  with  $V_{\text{LSR}} = +7.6$  km/s) regions, both  $1' \times 3'$  OTF maps. The size of the maps is about  $300'' \times 350''$ , covering both Ser-SMM1 and Ser-SMM3/Ser-SMM4 regions. The regions are referenced in the article as 'the Northern part' and 'the Southern part' respectively.

Data reduction was carried out with the CLASS package within GILDAS<sup>1</sup>. Each spectrum was corrected for the baseline shape, the spike channels were removed and the velocity was resampled to a resolution of 0.5 km/s. The baseline fitting of the order of 0 was sufficient for our observations. The rms of extracted spectra values vary from 0.024 K to 0.125 K. Both OTF maps were merged in one map covering  $300 \times 350$  arcsec. The spectra obtained were exported from the CLASS package and analysed with Python scripts.

### 2.2. Continuum emission

### 2.3. Physical properties of embedded protostars

Ten Class 0/I protostars are present in the observed region. There are deeply embedded sources so the radiation coming from their neighbourhood is highly absorbed in the envelopes, then re-emitted in the IR range. Envelopes become thinner with time due to outflow-envelope interactions (Arce & Sargent 2006). Class I sources SEDs are dominated by the emission in shorter wavelengths in respect to Class 0 objects. Thus Spectral Energy Distributions (SEDs) allow to estimate the evolutionary stage of an object (Andre et al. 1993).

Figure A.1 shows spectral energy distributions for all Class 0/I protostars in the region (Table 2). The SED plots include the selected literature samples (Dunham et al. 2015) combined with the data from the Herschel Gould Belt survey project (André et al. 2010). The additional Herschel data cover the SED peak, therefore provide a more detailed information allowing to calculate the bolometric temperatures and luminosities of the protostar more precisely.

Table 2 contains the observed protostars parameters as well as the classification from Enoch et al. 2009. Early Class 0 was

<sup>1</sup> See <http://www.iram.fr/IRAMFR/GILDAS>

Table 1: Overview of the observations

Mol.	Trans.	$\nu$ (GHz)	$E_u/k_B$ (K)	$A_{ul}$ ( $s^{-1}$ )	$g_u$	$n_{crit}$ ( $cm^{-3}$ )	Beam size ( $''$ )	Beam eff. $\eta_{MB}$
HCN	1-0	88.631602	4.25	$2.407 \times 10^{-5}$	3	$5.0 \times 10^6$ <sup>b</sup>	28	0.81
CN	1-0	113.494921	5.45	$1.182 \times 10^{-5}$	3	$1.1 \times 10^5$ <sup>c</sup>	22	0.78
CS	3-2	146.969029	14.1	$6.071 \times 10^{-5}$	7	$2.6 \times 10^5$ <sup>c</sup>	16	0.74
C <sup>34</sup> S	3-2	144.617109	13.9	$7.251 \times 10^{-5}$ <sup>a</sup>	7	$5.84 \times 10^{11}$ <sup>a</sup>	16	0.74
H <sup>13</sup> CN	1-0	86.342274	4.14	$1.512 \times 10^{-5}$ <sup>a</sup>	3	$9.7 \times 10^6$ <sup>b</sup>	29	0.81
H <sup>13</sup> CN	2-1	172.677881	12.43	$6.90 \times 10^{-5}$ <sup>a</sup>	5	$1.2 \times 10^6$ <sup>c</sup>	14	0.68

References: Molecular data adopted from LAMDA/JPL databases: <sup>a</sup> calculated for  $T = 300$  K; <sup>a</sup>Jiménez-Donaire et al. 2016, assuming optically thin transition lines for an excitation temperature of 20K; <sup>c</sup>Shirley 2015, assuming optically thin transition lines for an excitation temperature of 50K; <sup>d</sup>Chandra et al. 1995.

**Notes.** Beam sizes and efficiencies are taken from <http://www.iram.es/IRAMES/mainWiki/Iram30mEfficiencies>

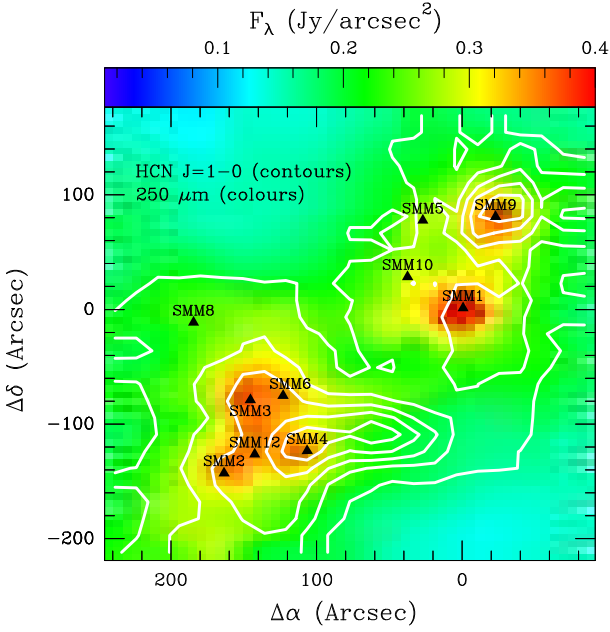


Fig. 1: Molecular emission of HCN  $J=1-0$  (contours) overplot on continuum emission *Herschel*/SPIRE (Griffin et al. 2010)  $250 \mu m$  (colours). Countours the lowest level is set on  $0.4$  K km/s ( $3\sigma$ ), step size of  $4$  K km/s.

defined as a protostar of bolometric temperature lesser than  $50$  K. Protostars characterised by bolometric temperature between  $50$  K and  $100$  K were classified as Late Class 0 protostars. Class I protostars were divided for Early and Late sub-type by the bolometric temperature of  $300$  K.

Most of the observed protostars in the Serpens Main region are very young, embedded sources of Early Class 0. SMM4, SMM10 and SMM12 are classified as Late Class 0 YSOs. The SMM5 and SMM6 protostars are the most evolved objects in our sample (Class I).

### 3. Results

#### 3.1. Molecular emission maps

The line maps in the targeted molecules show variety of structures that can be associated with YSOs and a large-scale cloud emission. Different spatial extend in molecules radiation is con-

nected with various physical conditions around protostars. Here, we present the large-scale maps of CS  $J = 3 - 2$ , HCN  $J = 1 - 0$  and CN  $J = 1 - 0$ . Maps of their isotopologues are shown in the Appendix A.

We present large-scale intensity maps (Fig. 2) of the targeted lines integrated at the level of  $3\sigma$  and above. Three of the observed molecules (HCN, CN and H<sup>13</sup>CN) are characterised by hyperfine structure. High resolution spectroscopy allow us to separate the emission from each hyperfine transitions. The integrated intensity maps of the lowest transitions of HCN, CN and H<sup>13</sup>CN are performed as a sum of all hyperfine splitting components. The maps are centred at  $\alpha_{J2000} = 18^h29^m46.6^s$ ,  $\delta_{J2000} = 01^\circ18'20.5''$ .

Most of molecular emission is concentrated in the SE subcluster, where 6 low-mass protostars are located, while the continuum emission peaks in the NW subcluster what is correlated with the other 4 low-mass protostars positions. The most extended structures can be associated with molecular outflows ejected from low-mass protostars (Table 2). Outflows directions were marked based on previous studies in CO transitions CO  $J = 3 - 2$  (Dionatos et al. 2010) and CO  $J = 6 - 5$ /CO  $J = 3 - 2$  (Yıldız et al. 2015). Five off-source positions were selected to detailed spectra analysis (Table 3).

The integrated line intensity map of HCN  $J = 1 - 0$  shows extended emission along outflow directions. This is the strongest line among all observed. The emission is slightly correlated with continuum emission. Most of the emission is associated with protostars positions. The HCN  $J = 1 - 0$  gas peaks around Ser-SMM9 and Ser-SMM4 protostars. There is no significant peak around strong submillimetre sources as Ser-SMM1 and Ser-SMM3. The low energy level of HCN ( $E_u = 4.25$  K) with the critical density of  $10^6$   $cm^{-2}$  traces cold, high-density gas. HCN has previously been shown to be a good tracer of molecular outflows activity (Lee et al. 2014). The HCN  $J = 1 - 0$  line was detected at all protostars positions, although it is weak at the positions of Ser-SMM5, Ser-SMM8 and Ser-SMM10. On the other hand, the HCN  $J = 1 - 0$  emission is particularly strong in Ser-SMM4 blue-shifted outflow (outflow position no. 4). NS elongated structure is present around Ser-SMM1 protostar what was noticed also in high- $J$  transitions (Yıldız et al. 2015). The emission is slightly extended along Ser-SMM9 outflows. There is no intensively elongated outflow structure from the other sources.

CS  $J = 3 - 2$  line emission map shows similar spatial distribution to HCN  $J = 1 - 0$ . Both species trace the gas of the same properties, however the CS molecule is excited in slightly less

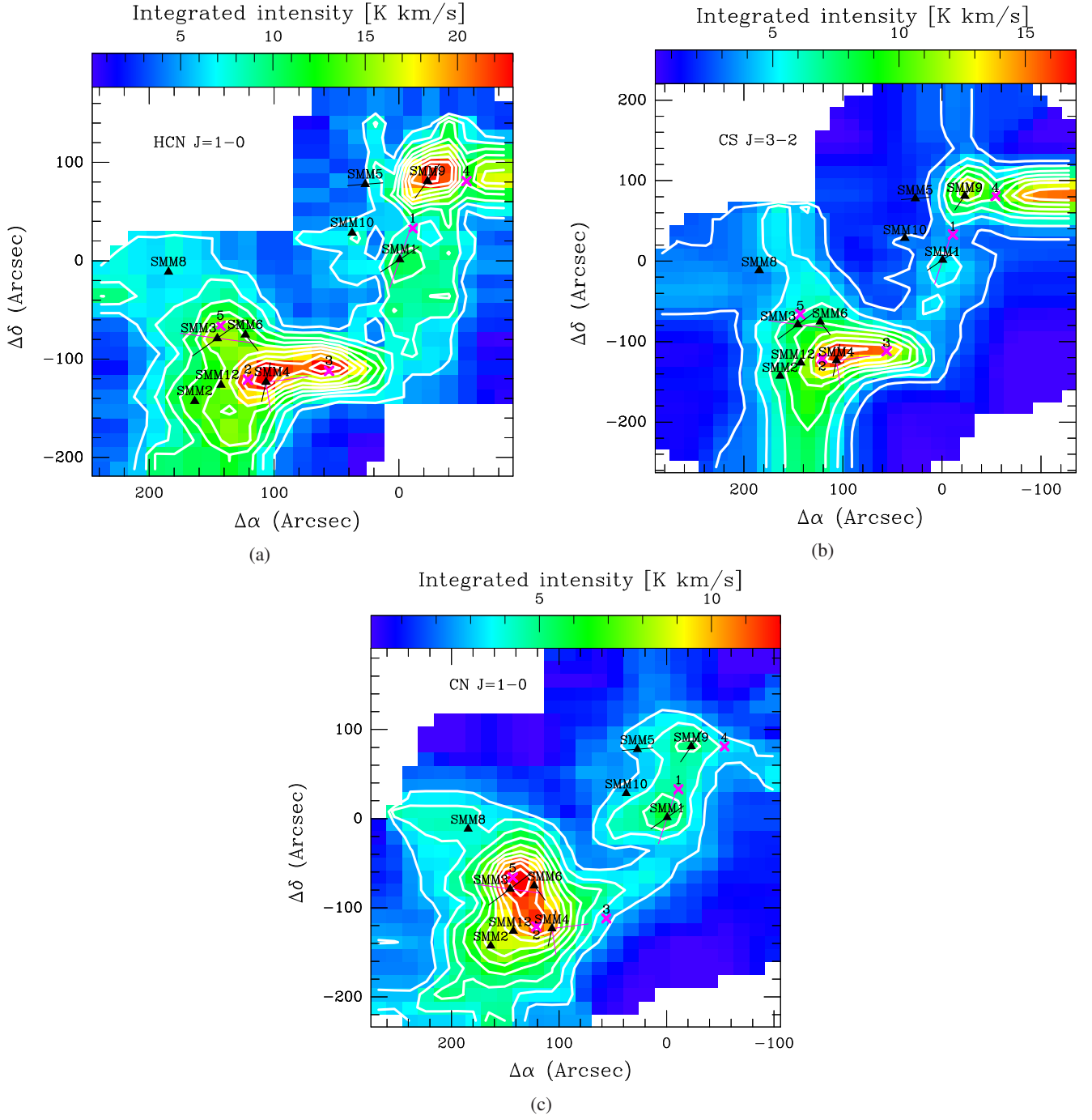


Fig. 2: Integrated intensity  $\int T_{\text{mb}} dV$  of the HCN  $J = 1 - 0$  (upper left panel), CS  $J = 3 - 2$  (upper right panel) and CN  $J = 1 - 0$  (bottom panel) in the Serpens Main region. The first contour at  $30 \sigma$  level, with step of  $10 \sigma$ , except CS  $J = 3 - 2$  line (b) where the first contour is at  $10 \sigma$  with step of  $5 \sigma$ . Black triangles show the positions of the protostars (Suresh et al. 2016), whereas the black lines (Yildiz et al. 2015) and magenta line (Dionatos et al. 2010) show the associated outflow directions. Outflow positions are displayed as magenta crosses.

dense environment ( $\sim 10^5 \text{ cm}^{-3}$ ). The most significant elongated structure can be associated with Ser-SMM4 blue-shifted outflow. It is situated at the same place in both maps, extending over  $80''$ . A similar large-scale structure is detected along Ser-SMM1 outflows, although it is stronger in the HCN  $J = 1 - 0$  map. Emission around Ser-SMM9 have a circular shape, however, there is additional elongated structure in CS  $J = 3 - 2$  line emission towards West. It overlaps with the S68N outflows seen in methanol observations (Kristensen et al. 2010). The HCN  $J = 1 - 0$  line

emission propagates for larger distances than the CS  $J = 3 - 2$ . It is also relatively stronger. In both cases the highest peak of the emission is situated around Ser-SMM4 protostar with a significant extent towards outflow position no. 3. Their weaker isotopic species  $\text{H}^{13}\text{CN } J = 1 - 0$  and  $\text{C}^{34}\text{S}(3-2)$  lines peak around the protostars position. The lines exhibits similar morphological distribution as HCN  $J = 1 - 0$  and CS  $J = 3 - 2$ .

CN  $J = 1 - 0$  line emission is focused mostly around the positions of protostars. The CN line is similarly low-energetic,



Table 2: Catalogue of protostars properties

Source (J2000.0)	R.A. (J2000.0)	Decl. (J2000.0)	$T_{\text{bol}}$ (K)	$L_{\text{bol}}$ ( $L_{\odot}$ )	Class	Other names
SMM9	18 29 48.3	+01 16 42.7	34.9	10.3	Early Class 0	Bolo22, Ser-emb8, ISO241, WMW23
SMM1	18 29 50.0	+01 15 20.3	35.4	78.7	Early Class 0	Bolo23, Ser-emb6, FIRS1, EC41
SMM5	18 29 51.4	+01 16 38.3	150.5	3.7	Early Class I	Bolo22, Ser-emb21, EC53, WMW24, Ser p3
SMM10	18 29 52.3	+01 15 48.8	82.6	6.2	Late Class 0	Bolo 23, Ser-emb12, WMW21
SMM4	18 29 57.0	+01 13 11.3	76.9	4.4	Late Class 0	Bolo25, Ser-emb22
SMM6	18 29 57.8	+01 14 05.3	532.3	43.1	Late Class I	Bolo 28, Ser-emb30, EC90, WMW35, SVS20S
SMM12	18 29 59.1	+01 13 14.3	96.9	5.7	Late Class 0	Bolo28, Ser-emb19
SMM3	18 29 59.6	+01 13 59.2	35.0	6.9	Early Class 0	Bolo26, Ser-emb26
SMM2	18 30 00.5	+01 12 57.8	30.5	4.07	Early Class 0	Bolo28, Ser-emb4
SMM8	18 30 01.9	+01 15 09.2	15.3	0.2	Early Class 0	Bolo30

Coordinates taken from [Suresh et al. 2016](#), except SMM8 ([Lee et al. 2014](#)).

Table 3: Properties of the selected off-source positions

Pos.	R.A. (J200)	Decl. (J200)	Remarks
1	18:29:45.47	+01:15:53.5	SMM1 blue-shifted outflow in CO $J = 3 - 2$
2	18:29:54.66	+01:13:19.5	max. CN $J = 1 - 0$ , SMM4 blue-shifted outflow in CO $J = 3 - 2$
3	18:29:50.33	+01:13:68.5	max. HCN $J = 1 - 0$ , SMM4 blue-shifted
4	18:29:43	+01:16:41.5	outflow visible in C <sup>34</sup> S(3-2)
5	18:29:56.13	+01:14:14.5	max. CN $J = 1 - 0$ , SMM9 surroundings

however it peaks in different areas than HCN and CS. The CN  $J = 1 - 0$  integrated intensity structures follow the  $250 \mu\text{m}$  continuum map. The highest local peaks are associated with Class 0 low-mass protostars: Ser-SMM3, Ser-SMM4 and Ser-SMM6, as well as local maxima around Ser-SMM1 and Ser-SMM9. The spatial distribution is qualitatively different compared to the HCN  $J = 1 - 0$  and CS  $J = 3 - 2$  maps. The strongest emission characterises the dense surroundings of protostars in SE subcluster while the NW subcluster does not show such a distinct emission as in the HCN  $J = 1 - 0$  line. Dense emissive region of the Ser-SMM9 source is significantly weaker in CN  $J = 1 - 0$  line. CN  $J = 1 - 0$  map can be characterised by compact, condensed emission without any strongly elongated structures.

### 3.2. Comparison of the spatial extent of CN and HCN

We present a large-scale map of CN  $J = 1 - 0$  and HCN  $J = 1 - 0$  integrated intensity (Fig. 3) showing the emission exceeding  $30 \sigma$  for both molecules. The image of CN emission has been resampled to beam size of HCN in order to compare the same emitting regions.

The CN  $J = 1 - 0$  transition is shifted to the north in respect to the HCN  $J = 1 - 0$  emission. It is highly concentrated in the SE subcluster, while the NW subcluster is dominated by the HCN. Both molecules show a diffusive ‘bridge’ between the two subclusters. In HCN it is connected with Ser-SMM4 and Ser-SMM1 outflows, while the CN follows the dust continuum emission. The emission in both molecules is anti-correlated north from Ser-SMM6 and west from Ser-SMM4 sources. At the dense area of Ser-SMM9 surrounding CN/HCN ratio is significantly weaker.

Both species has been detected in all sources positions. CN as a product of HCN photodissociation indicates other properties of low-mass protostars surroundings (Section 4). The highest CN/HCN integrated intensity ratio occurs in Ser-SMM6 and Ser-SMM3s protostars, as well as in the outflow position no. 5. On the other hand, Ser-SMM9 object is characterised by very low CN/HCN line ratio. Similarly low CN/HCN ratio is measured in outflow positions no. 3 and 4. Most of the sources show high flux values in both molecules (Table 4). However, they present unequal levels which indicates regions of different properties. In order to better understand this issue we analyse the molecular line profiles in the Section 3.2.

The low energy level of HCN ( $E_u = 4.25 \text{ K}$ ) traces cold, high-density gas. HCN has previously been shown to be a good tracer of molecular outflows activity ([Walker-Smith et al. 2014](#)).

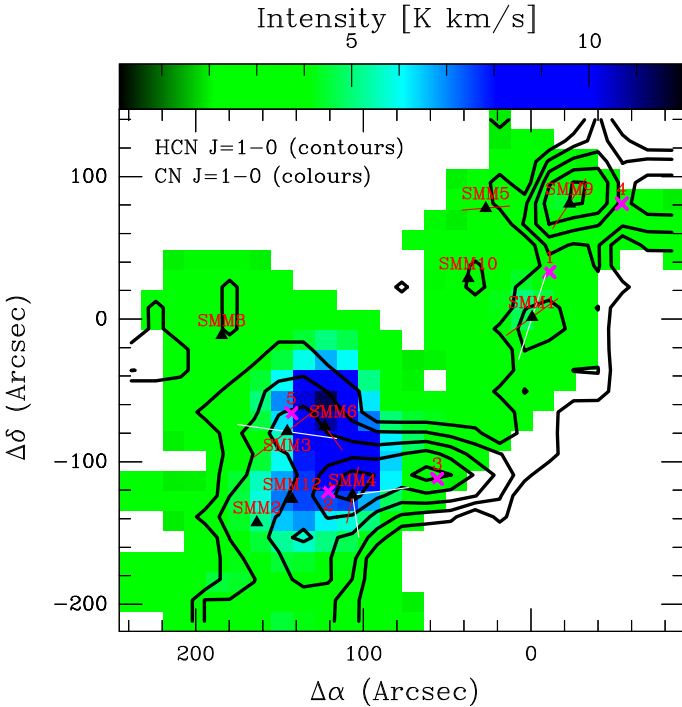


Fig. 3: Integrated intensity  $\int T_{\text{mb}} dV$  of CN  $J = 1 - 0$  (colours) and HCN  $J = 1 - 0$  (contours) in the Serpens Main region. The first contour is 30. Triangles and lines marked as described in 2.

Table 4: CN/HCN integrated intensities

Source	$\int T_{mb} dV _{CN}$ (K km/s)	$\int T_{mb} dV _{HCN}$ (K km/s)	CN/HCN
SMM1	5.26	8.23	0.64
SMM2	8.41	12.57	0.67
SMM3	13.18	14.14	0.93
SMM4	9.89	17.59	0.56
SMM5	3.49	5.79	0.60
SMM6	10.57	11.85	0.89
SMM8	5.09	6.32	0.81
SMM9	5.41	14.08	0.38
SMM10	2.59	6.96	0.37
SMM12	9.10	13.27	0.69
Outflow1	4.8	8.3	0.58
Outflow2	11.2	21.4	0.52
Outflow3	3.8	23.6	0.16
Outflow4	3.7	12.4	0.3
Outflow5	13.3	14.9	0.89

Similar spatial distribution is presented in the CS map. It means that both species trace the gas of the same properties. The CN line is similarly low-energetic, however it peaks in different areas than HCN and CS. CN as a product of HCN photodissociation indicates other properties of low-mass protostars surroundings (Section 4).

Spatial distribution of different lines emission varies depending on the observed molecule. The most distinct differences can be noticed between HCN and CN map. However, they present unequal levels which indicates regions of different properties. In order to better understand this issue we analyse the molecular line profiles in the Section 3.2.

### 3.3. Line profiles

We selected 14 representative on-source and off-source positions for a detailed analysis (Fig. ??). Nine of them are corresponding to the protostars positions, the other five off-source positions were selected based on local maximum of the flux.

In the majority of our sources five of targeted lines were detected: CN  $J = 1 - 0$ , HCN  $J = 1 - 0$ , CS  $J = 3 - 2$ , C<sup>34</sup>S  $J = 3 - 2$  and H<sup>13</sup>CN  $J = 1 - 0$ . The line is considered to be detected if there is an emission at the level of at least  $3\sigma$ . A weak emission from H<sup>13</sup>CN  $J = 2 - 1$  was found at the positions of four sources and it is not included in Fig. ??.

The strongest emission occurs in HCN  $J = 1 - 0$ , CN  $J = 1 - 0$  and CS  $J = 3 - 2$  lines and it was detected at the position of all of the sources. The emission in the other lines was multiplied in order to compare profiles between different molecules. In HCN, CN species and their isotopologues a few different velocity components can be identified what indicates the hyperfine splitting. This occurs if a molecule has a non-zero nuclear spin so there is also an interaction between the nuclear spin and the electronic angular momentum. The most distinct splitting can be spotted in the CN  $J = 1 - 0$  profiles with five separate components situated between -70 km/s and 18 km/s. The HCN  $J = 1 - 0$  line is characterised by three components with low separation situated in the range of -2 km/s – 16 km/s.

Ser-SMM1, Ser-SMM9, and Ser-SMM10 sources have wide spectral lines, while others exhibit narrow line profiles. Spectra extracted from Outflows no. 1, 4 and 5 shows prominent blue-

shifted wings. Similar structure can be noticed in the Ser-SMM3 (panel no. 7) CS 3-2 and HCN  $J = 1 - 0$  profiles.

## 4. Analysis

### 4.1. Lines column densities

Table 6 shows fluxes integrated from the average line profile at the positions of known protostars. Flux calculation in individual lines allows us to determine the column density of a given transition. The column density of the upper level  $N_u$  of each observed line was calculated based on following relation:

$$N_u = \beta \frac{\nu W}{A} \quad (1)$$

where  $\beta = 1937 \text{ cm}^{-2}$  and  $W = \int T_{mb} dV$  is the integrated intensity of the emission line. The frequency  $\nu$  should be given in GHz. The total column density was obtained using:

$$N_{tot} = Q(T_{ex}) \exp\left(\frac{E_u}{k T_{ex}}\right) \frac{N_u}{g_u} \quad (2)$$

where is the partition function depending on excitation temperature  $T_{ex}$  and  $k$  Boltzmann constant.

The column densities of the upper level of CN  $J = 1 - 0$  and HCN  $J = 1 - 0$  transitions are presented in Table 6. The lowest transition of CN is more abundant molecule than the lowest transition line of HCN at the low-mass protostars positions. The column density of CN  $J = 1 - 0$  varies between  $10^{14} - 10^{15} \text{ cm}^{-2}$ , while in the column density of the HCN's lowest transition reaches  $10^{14} \text{ cm}^{-2}$ . In the case of Ser-SMM2, Ser-SMM3, Ser-SMM4, Ser-SMM6 and Ser-SMM12 HCN  $J = 1 - 0$  line column density is an order of magnitude lower than the column density of the equivalent CN transition. This result provides a clue to better understand of the low-mass protostars chemistry.

### 4.2. RADEX modelling

Column densities can be independently determined using molecular excitation models. Line ratio can provide additional information concerning physical properties of the observed gas.

The non-LTE radiative transfer code RADEX (van der Tak et al. 2007) was run in order to prepare sets of molecular excitation models. The CN and HCN molecules column density ratio, hydrogen number density and kinetic temperature of the gas were free parameters. HCN column density was chosen as  $10^8 \text{ cm}^{-2}$  in order to ensure optically thin emission. CN column density parameter varies from  $10^6 \text{ cm}^{-2}$  to  $10^{10} \text{ cm}^{-2}$  what translates into  $N_{CN}/N_{HCN}$  in following limits:  $10^{-2} - 10^2$ . The sets of models were obtained assuming a line width of  $1.0 \text{ km s}^{-1}$ , hydrogen densities of  $n_{H_2} = 10^3 \text{ cm}^{-3}$ ,  $n_{H_2} = 10^4 \text{ cm}^{-3}$  and  $n_{H_2} = 10^5 \text{ cm}^{-3}$  and kinetic temperatures of  $T_{kin} = 30 \text{ K}$ ,  $T_{kin} = 75 \text{ K}$  and  $T_{kin} = 200 \text{ K}$ . The molecular data files used during modelling were procured from the Leiden Atomic and Molecular Database (LAMDA, Schöier et al. 2005).

Fig. 5 presents one exemplary set of models of CN/HCN column density ratio versus the modelled line intensities ratio for hydrogen densities of  $n_{H_2} = 10^5 \text{ cm}^{-3}$  and kinetic temperatures of  $T_{kin} = 200 \text{ K}$ . The rest of the models are shown in the Appendix B. CN/HCN column density ratio weakly depends on hydrogen density and kinetic temperature in the low limit of those parameters. All presented models show similar properties.

The modelled line intensities are compared with the observations. The observed line intensity ratio covers a range of 0.0-1.0

Table 5: Patterns of emission in molecular species

Source	HCN $J = 1 - 0$	CN $J = 1 - 0$	Remarks
SMM1	rb	c	multiple system of 5 components <sup>a</sup>
SMM2	b	b	multiple system of 3 components <sup>b</sup>
SMM3	b	b	
SMM4	rb	rb	binary <sup>c</sup>
SMM5	x	x	variable <sup>d</sup>
SMM5	x	x	
SMM8	r	r	
SMM9	rb	r	
SMM10	x	x	
SMM12	b	b	

References: <sup>a</sup> Hull et al. (2017), <sup>b</sup> Francis et al. (2019), <sup>c</sup> Aso et al. (2018), <sup>d</sup> Yoo et al. (2017).

of the column density ratio in the logarithmic scale. That corresponds to a few times higher CN column density than the same parameter of HCN. This result slightly depends on hydrogen densities and kinetic temperature of the gas (see Table 7).

## 5. Discussion

### 5.1. Astrochemical model

In Section 3.2 we have raised a question about influence of the UV radiation on the surrounding of the observed sources. A simply astrochemical model can be obtained in order to estimate the intensity of the UV field in reference to units of the interstellar UV field  $G_0$ .

HCN easily photodissociates into CN molecule and H atom. On the other hand, CN needs more energetic photon for disintegration. This leads to higher abundance of CN molecules and increases CN/HCN column density ratio.

We used Nahoon code that model the time evolution of 474 species involving gas-phase and gas-grain reactions with fixed temperature, density, UV, and cosmic ray fluxes (Wakelam et al. 2012). The evolution of CN, HCN and CS abundances was started at the time of a dense cloud formation. The UV radiation is described through the relation between visual extinction  $A_V$  and the photodissociation rate coefficient  $k$  Eq A.3:

$$k = \alpha e^{-\gamma A_V} \quad (3)$$

Here,  $\alpha$  and  $\gamma$  are coefficients of photodissociation HCN equal  $1.64 \times 10^{-9}$  and 3.12 respectively (Heays et al. (2017)).

Figure 6 shows a model corresponding to a typical dense cloud with temperature of 10 K and hydrogen total density of  $n_{\text{H}+\text{H}_2} = 10^4 \text{ cm}^{-3}$ . The chemical composition of the studied molecules stabilises at the time of  $10^7$  yrs with HCN abundance higher with respect to CN. We assumed the time of  $10^6$  yrs as the time when the star formation starts in dense clouds. The modelled abundances of the all 474 species at the time of  $10^6$  yrs were used as an input data for the following set of models.

Based on the initial abundances of all species from starless cloud modelling, the closest neighbourhood of low-mass protostars was simulated. We adopted the UV radiation and cosmic ray fluxes typical for dense clouds as an initial conditions. The visual extinction and the total cosmic-ray ionization rate were set as 5 mag and  $1.3 \times 10^{17} \text{ s}^{-1}$  respectively. The sets of models were run for the temperature range between 10 and 200 K and the total hydrogen densities from  $10^4 \text{ cm}^{-3}$  to  $10^6 \text{ cm}^{-3}$ . The resulting ratio of CN and HCN abundances is shown in Fig. 7. The results

are consistent with starless cloud model (Fig. 6). Without any additional source of the UV radiation the HCN is more abundant molecule than CN about 2-3 orders of magnitude. Moreover, the CN/HCN abundances ratio is slightly dependent on gas temperature up to 150 K.

This results justify assumptions for the modelling the neighbourhood of low-mass protostars with the fixed gas temperature of 50 K. The models were run for the range of visual extinction between  $1^m$  and  $2.1^m$  what corresponds to the UV radiation field of 0.044 to 0.001  $G_0$ . The computed CN/HCN abundances ratio is presented in Fig. 8. The additional UV radiation of the strength of few thousandth of the average interstellar UV radiation field is enough to cover the observations in wide range of total hydrogen densities.

An additional source of the UV radiation was needed to reproduce the observational CN/HCN abundances what leads to conclusion that there is non-zero UV radiation field around low-mass protostars.

## 6. Conclusions

**Acknowledgements.** AM, AK and MG are supported by the Polish National Science Center grants NAVA InterAPS and 2016/21/D/ST9/01098. This research has made use of data from the Herschel Gould Belt survey (HGBS) project (<http://gouldbelt-herschel.cea.fr>). The HGBS is a Herschel Key Programme jointly carried out by SPIRE Specialist Astronomy Group 3 (SAG 3), scientists of several institutes in the PACS Consortium (CEA Saclay, INAF-IFSI Rome and INAF-Arcetri, KU Leuven, MPIA Heidelberg), and scientists of the Herschel Science Center (HSC).

## References

- André, P., Men'shchikov, A., Bontemps, S., et al. 2010, A&A, 518, L102
- Andre, P., Ward-Thompson, D., & Barsony, M. 1993, ApJ, 406, 122
- Arce, H. G. & Sargent, A. I. 2006, ApJ, 646, 1070
- Aso, Y., Hirano, N., Aikawa, Y., et al. 2018, ApJ, 863, 19
- Bachiller, R., Pérez Gutiérrez, M., Kumar, M. S. N., & Tafalla, M. 2001, A&A, 372, 899
- Bergin, E. A. & Tafalla, M. 2007, ARA&A, 45, 339
- Casali, M. M., Eiroa, C., & Duncan, W. D. 1993, A&A, 275, 195
- Chapillon, E., Guilloteau, S., Dutrey, A., Piétu, V., & Guélin, M. 2012, A&A, 537, A60
- Davis, C. J., Matthews, H. E., Ray, T. P., Dent, W. R. F., & Richer, J. S. 1999, MNRAS, 309, 141
- Di Francesco, J., Johnstone, D., Kirk, H., MacKenzie, T., & Ledwosinska, E. 2008, ApJS, 175, 277
- Dionatos, O., Nisini, B., Codella, C., & Giannini, T. 2010, A&A, 523, A29
- Dunham, M. M., Allen, L. E., Evans, Neal J., I., et al. 2015, ApJS, 220, 11
- Enoch, M. L., Evans, Neal J., I., Sargent, A. I., & Glenn, J. 2009, ApJ, 692, 973
- Enoch, M. L., Glenn, J., Evans, Neal J., I., et al. 2007, ApJ, 666, 982

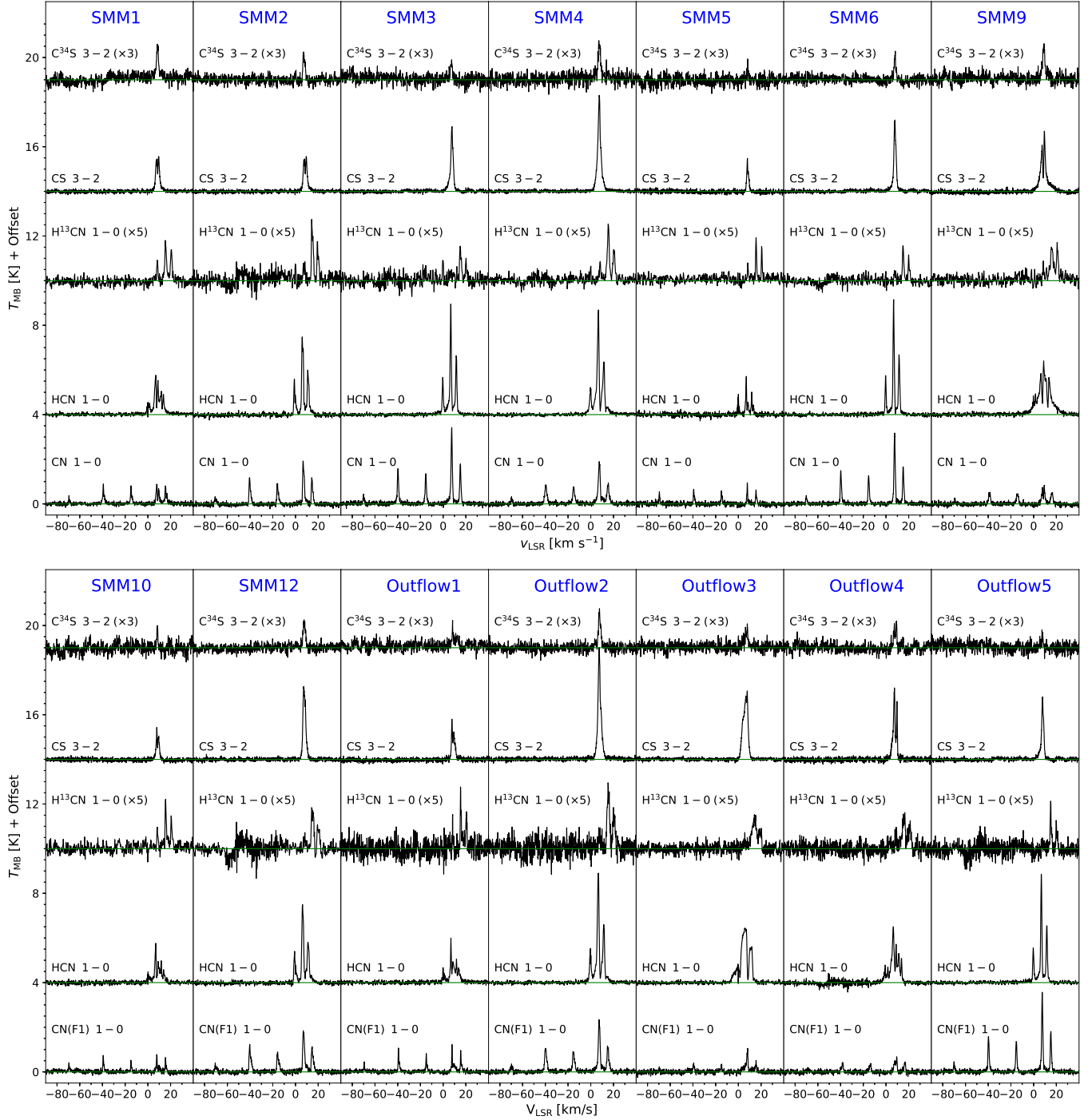


Fig. 4: Serpens Main sources spectra of  $\text{C}^{34}\text{S } J = 3 - 2$ ,  $\text{CS } J = 3 - 2$ ,  $\text{H}^{13}\text{CN } J = 1 - 0$ ,  $\text{HCN } J = 1 - 0$  and  $\text{CN } J = 1 - 0$  lines.

Evans, Neal J., I., Allen, L. E., Blake, G. A., et al. 2003, *PASP*, 115, 965  
 Evans, Neal J., I., Dunham, M. M., Jørgensen, J. K., et al. 2009, *ApJS*, 181, 321  
 Francis, L., Johnstone, D., Dunham, M. M., Hunter, T. R., & Mairs, S. 2019, *ApJ*, 871, 149  
 Fuente, A., Martin-Pintado, J., Cernicharo, J., & Bachiller, R. 1993, *A&A*, 276, 473  
 Fuente, A., Martin-Pintado, J., & Gaume, R. 1995, *ApJ*, 442, L33  
 Green, J. D., Evans, Neal J., I., Jørgensen, J. K., et al. 2013, *ApJ*, 770, 123  
 Harvey, P., Merín, B., Huard, T. L., et al. 2007, *ApJ*, 663, 1149  
 Heays, A. N., Bosman, A. D., & van Dishoeck, E. F. 2017, *A&A*, 602, A105  
 Hogerheijde, M. R., van Dishoeck, E. F., Salverda, J. M., & Blake, G. A. 1999, *ApJ*, 513, 350  
 Hull, C. L. H., Girart, J. M., Tychoniec, Ł., et al. 2017, *ApJ*, 847, 92  
 Hurt, R. L. & Barsony, M. 1996, *ApJ*, 460, L45  
 Jørgensen, J. K. 2004, *A&A*, 424, 589

Karska, A., Herczeg, G. J., van Dishoeck, E. F., et al. 2013, *A&A*, 552, A141  
 Karska, A., Kaufman, M. J., Kristensen, L. E., et al. 2018, *ApJS*, 235, 30  
 Karska, A., Kristensen, L. E., van Dishoeck, E. F., et al. 2014, *A&A*, 572, A9  
 Kristensen, L. E., van Dishoeck, E. F., Mottram, J. C., et al. 2017, *A&A*, 605, A93  
 Kristensen, L. E., van Dishoeck, E. F., van Kempen, T. A., et al. 2010, *A&A*, 516, A57  
 Kroupa, P. 2002, *Science*, 295, 82  
 Lada, C. J. 1987, in *IAU Symposium*, Vol. 115, *Star Forming Regions*, ed. M. Peimbert & J. Jugaku, 1  
 Larson, R. B. 2003, *Reports on Progress in Physics*, 66, 1651  
 Lee, K. I., Fernández-López, M., Storm, S., et al. 2014, *ApJ*, 797, 76  
 Manoj, P., Watson, D. M., Neufeld, D. A., et al. 2013, *ApJ*, 763, 83  
 McMullin, J. P., Mundy, L. G., Blake, G. A., et al. 2000, *ApJ*, 536, 845  
 Myers, P. C. & Ladd, E. F. 1993, *ApJ*, 413, L47



Table 6: Integrated fluxes of the observed line at the positions of protostars

Source	Line	$\int T_{mb} dV$ (K km/s)	$T_{peak}$ (K)	$N_{up}$ (cm <sup>-2</sup> )	$N_{tot}$ (cm <sup>-2</sup> )
SMM1	CN 1-0	5.26	0.89	$1.1 \times 10^{13}$	$6.6 \times 10^{14}$
	HCN 1-0	8.23	1.76	$5.2 \times 10^{12}$	$2.0 \times 10^{14}$
	CS 3-2	2.98	1.57	$2.1 \times 10^{12}$	$2.3 \times 10^{13}$
	C <sup>34</sup> S 3-2	1.21	0.56		
	H <sup>13</sup> CN 1-0	1.43	0.45		
SMM2	CN 1-0	8.41	1.92	$1.8 \times 10^{13}$	$1.1 \times 10^{15}$
	HCN 1-0	12.57	3.48	$8.0 \times 10^{12}$	$3.0 \times 10^{12}$
	CS 3-2	6.57	3.10	$4.5 \times 10^{12}$	$2.0 \times 10^{13}$
	C <sup>34</sup> S 3-2	0.89	0.47		
	H <sup>13</sup> CN 1-0	1.65	0.64		
SMM3	CN 1-0	13.18	3.42	$2.8 \times 10^{13}$	$1.7 \times 10^{15}$
	HCN 1-0	14.14	4.95	$8.9 \times 10^{12}$	$3.4 \times 10^{14}$
	CS 3-2	8.11	2.90	$5.6 \times 10^{13}$	$6.2 \times 10^{13}$
	C <sup>34</sup> S 3-2	0.604	0.36		
	H <sup>13</sup> CN 1-0	0.88	0.41		
SMM4	CN 1-0	9.89	1.90	$2.1 \times 10^{13}$	$1.3 \times 10^{15}$
	HCN 1-0	17.59	4.69	$1.1 \times 10^{13}$	$4.2 \times 10^{14}$
	CS 3-2	14.4	4.30	$9.9 \times 10^{12}$	$1.1 \times 10^{14}$
	C <sup>34</sup> S 3-2	1.56	0.64		
	H <sup>13</sup> CN 1-0	1.83	0.61		
SMM5	CN 1-0	3.49	0.94	$7.3 \times 10^{12}$	$4.4 \times 10^{14}$
	HCN 1-0	5.79	1.72	$3.7 \times 10^{12}$	$1.4 \times 10^{14}$
	CS 3-2	2.61	1.48	$1.8 \times 10^{12}$	$2.0 \times 10^{13}$
	C <sup>34</sup> S 3-2	0.28	0.42		
	H <sup>13</sup> CN 1-0	1.16	0.42		
SMM6	CN 1-0	10.57	3.17	$2.2 \times 10^{13}$	$1.3 \times 10^{15}$
	HCN 1-0	11.85	5.15	$8.9 \times 10^{12}$	$3.3 \times 10^{14}$
	CS 3-2	7.86	3.2	$5.4 \times 10^{12}$	$6.0 \times 10^{13}$
	C <sup>34</sup> S 3-2	0.74	0.56		
	H <sup>13</sup> CN 1-0	0.81	0.40		
SMM8	CN 1-0	5.09	0.94	$1.1 \times 10^{13}$	$6.4 \times 10^{14}$
	HCN 1-0	6.32	1.72	$4.0 \times 10^{12}$	$1.5 \times 10^{14}$
	CS 3-2	4.64	2.08	$3.2 \times 10^{12}$	$3.5 \times 10^{13}$
	C <sup>34</sup> S 3-2	0.22	0.35		
	H <sup>13</sup> CN 1-0	0.46	0.21		
SMM9	CN 1-0	5.41	0.84	$1.1 \times 10^{13}$	$6.8 \times 10^{14}$
	HCN 1-0	14.08	2.40	$8.9 \times 10^{12}$	$3.4 \times 10^{14}$
	CS 3-2	9.85	2.70	$6.8 \times 10^{12}$	$7.5 \times 10^{13}$
	C <sup>34</sup> S 3-2	1.3	0.62		
	H <sup>13</sup> CN 1-0	1.57	0.38		
SMM10	CN 1-0	2.59	0.78	$5.4 \times 10^{12}$	$3.3 \times 10^{14}$
	HCN 1-0	6.96	1.75	$4.4 \times 10^{12}$	$1.7 \times 10^{14}$
	CS 3-2	3.83	1.43	$2.6 \times 10^{12}$	$2.9 \times 10^{13}$
	C <sup>34</sup> S 3-2	0.56	0.40		
	H <sup>13</sup> CN 1-0	0.98	0.45		
SMM12	CN 1-0	9.10	1.85	$1.9 \times 10^{13}$	$1.2 \times 10^{15}$
	HCN 1-0	13.27	3.50	$8.4 \times 10^{12}$	$3.2 \times 10^{14}$
	CS 3-2	9.75	3.26	$6.7 \times 10^{12}$	$7.4 \times 10^{13}$
	C <sup>34</sup> S 3-2	1.18	0.58		
	H <sup>13</sup> CN 1-0	1.43	0.46		

Ortiz-León, G. N., Dzib, S. A., Kounkel, M. A., et al. 2017, *ApJ*, 834, 143  
Riaz, B., Thi, W. F., & Caselli, P. 2018, *MNRAS*, 481, 4662  
Schöier, F. L., van der Tak, F. F. S., van Dishoeck, E. F., & Black, J. H. 2005, *A&A*, 432, 369  
Skrutskie, M. F., Cutri, R. M., Stiening, R., et al. 2006, *AJ*, 131, 1163

Spaans, M., Hogerheijde, M. R., Mundy, L. G., & van Dishoeck, E. F. 1995, *ApJ*, 455, L167  
Stäuber, P., Benz, A. O., Jørgensen, J. K., et al. 2007, *A&A*, 466, 977  
Suresh, A., Dunham, M. M., Arce, H. G., et al. 2016, *AJ*, 152, 36  
Testi, L. & Sargent, A. I. 1998, *ApJ*, 508, L91

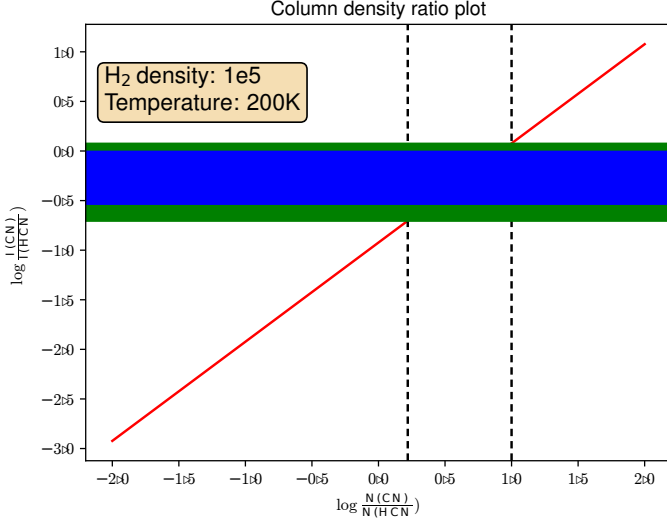


Fig. 5: CN/HCN column density ratio for hydrogen densities of  $n_{\text{H}_2} = 10^5 \text{ cm}^{-3}$  and kinetic temperatures of  $T_{\text{kin}} = 200 \text{ K}$  (red line). The observed line intensity ratio is plotted in blue (protostars positions) and green (all positions).

Table 7: CN/HCN column density ratio

$n_{\text{H}_2}$ ( $\text{cm}^{-3}$ )	$T_{\text{kin}}$ (K)	$\log_{10}(N[\text{CN}]/N[\text{HCN}])$
$10^3$	30	0.03-0.88
$10^3$	75	0.06-0.84
$10^3$	200	0.00-0.78
$10^4$	30	0.16-0.94
$10^4$	75	0.08-0.86
$10^4$	200	0.04-0.82
$10^5$	30	0.20-0.98
$10^5$	75	0.18-0.86
$10^5$	200	0.22-1.00

van der Tak, F. F. S., Black, J. H., Schöier, F. L., Jansen, D. J., & van Dishoeck, E. F. 2007, A&A, 468, 627  
van Dishoeck, E. F., Kristensen, L. E., Benz, A. O., et al. 2011, PASP, 123, 138  
van Kempen, T. A., van Dishoeck, E. F., Güsten, R., et al. 2009, A&A, 507, 1425  
Wakelam, V., Herbst, E., Loison, J. C., et al. 2012, ApJS, 199, 21  
Walker-Smith, S. L., Richer, J. S., Buckle, J. V., Hatchell, J., & Drabek-Maunders, E. 2014, MNRAS, 440, 3568  
Wright, E. L., Eisenhardt, P. R. M., Mainzer, A. K., et al. 2010, AJ, 140, 1868  
Yıldız, U. A., Kristensen, L. E., van Dishoeck, E. F., et al. 2015, A&A, 576, A109  
Yoo, H., Lee, J.-E., Mairs, S., et al. 2017, ApJ, 849, 69  
Zuckerman, B., Kuiper, T. B. H., & Rodriguez Kuiper, E. N. 1976, ApJ, 209, L137

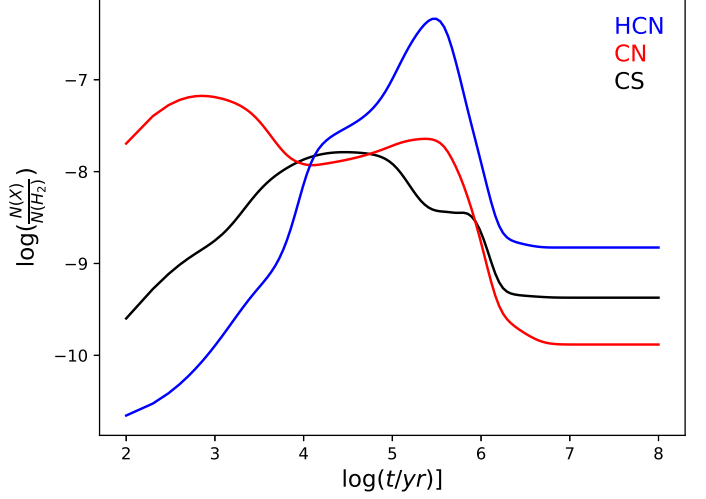


Fig. 6: Time evolution of CN (red line), HCN (blue line) and CS (black line) abundances obtained with Nohoon astrochemical code with initial parameters of  $n_{\text{HI}+2\text{H}_2} = 10^4 \text{ cm}^{-3}$ ,  $T = 10 \text{ K}$ ,  $A_V = 5 \text{ mag}$ . The assumed cosmic-ray ionization rate is  $1.3 \times 10^{17} \text{ s}^{-1}$ , dust to gas mass ratio is 0.01, dust grain radius is  $10^{-5} \text{ cm}$ , grain density is  $3 \text{ g cm}^{-3}$ .

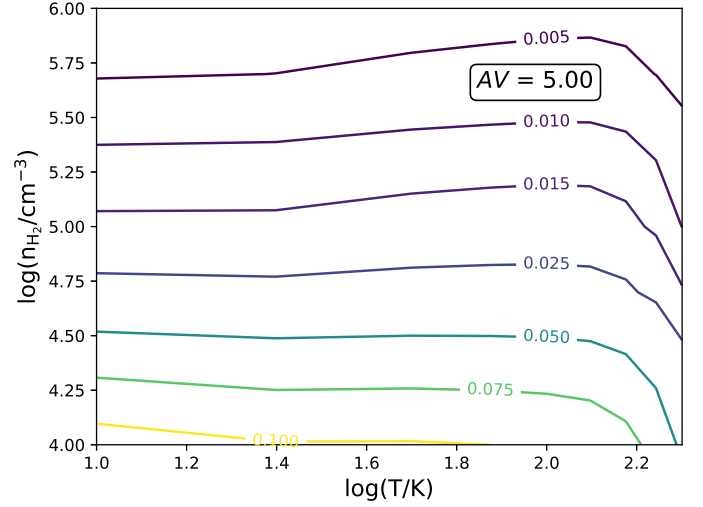


Fig. 7: Contour plot of Nohoon sets of models of CN/HCN abundances ratio with fixed visual extinction  $A_V = 5 \text{ mag}$  at the time of  $10^7 \text{ yrs}$  after star formation began in the cloud.

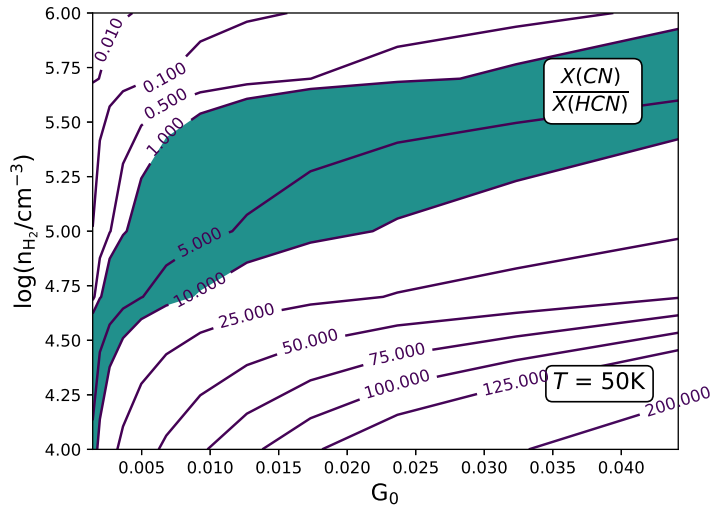


Fig. 8: Similar to Fig. 7 but for fixed temperature  $T = 50$  K.

## Appendix A: Spectral Energy Distributions

Broad-band observations are needed in order to determine physical properties of a protostar. Dunham et al. 2015 studied properties of protostars in the Serpens molecular cloud using 2MASS (Skrutskie et al. 2006) and Spitzer IRAC/MIPS (Evans et al. 2009), observations covering the range of 1.25–70  $\mu\text{m}$ , photometry from Wide-field Infrared Survey Explorer 12 and 22  $\mu\text{m}$  (WISE; Wright et al. 2010), SHARC-II 350  $\mu\text{m}$  (Suresh et al. 2016), the SCUBA Legacy Catalog 450 and 850  $\mu\text{m}$  (Di Francesco et al. 2008) and 1.1 mm observations from Bolocam dust survey (Enoch et al. 2007). The Serpens Main region was also observed during the Herschel Gould Belt survey project (André et al. 2010). SPIRE/PACS photometry in the Serpens molecular cloud is discussed in Fiorellino et al. (in prep.).

Based on SEDs the bolometric temperature and luminosity can be calculated for each of the observed protostars. The bolometric luminosity was determined by integrating the SEDs over frequency:

$$L_{bol} = \pi d^2 \int F_\nu d\nu \quad (\text{A.1})$$

where  $d$  is the cloud distance of  $436 \pm 9.2$  pc (Ortiz-León et al. 2017). The bolometric temperature was calculating as described in Myers & Ladd 1993:

$$T_{bol} = 1.25 \cdot 10^{-11} \bar{\nu} \quad (\text{A.2})$$

where  $\bar{\nu}$  is the mean frequency given by:

$$\bar{\nu} = \frac{\int \nu F_\nu d\nu}{\int F_\nu d\nu} \quad (\text{A.3})$$

Using Scipy *splrep* and *splev* functions cubic smooth spline interpolation of the photometric data was performed while calculating the protostars parameters. Integration along the resulting axis was obtain with the composite trapezoidal rule (*Scipy* package). The photometric data allows us to perform the integration along wide range of wavelength with exception of SMM8. Here we have only 4 photometric points from the Herschel Gould Belt so the calculated bolometric luminosity and temperature can be underestimated.

## Appendix B: Molecular emission maps

## Appendix C: Flux correlations

## Appendix D: Wings emission

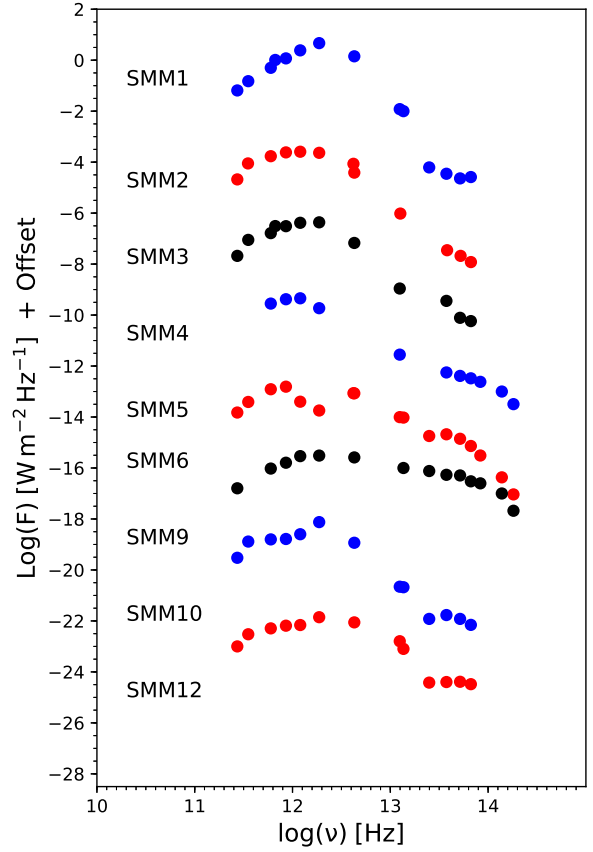


Fig. A.1: Spectral Energy Distributions of protostars in the Serpens Main region.

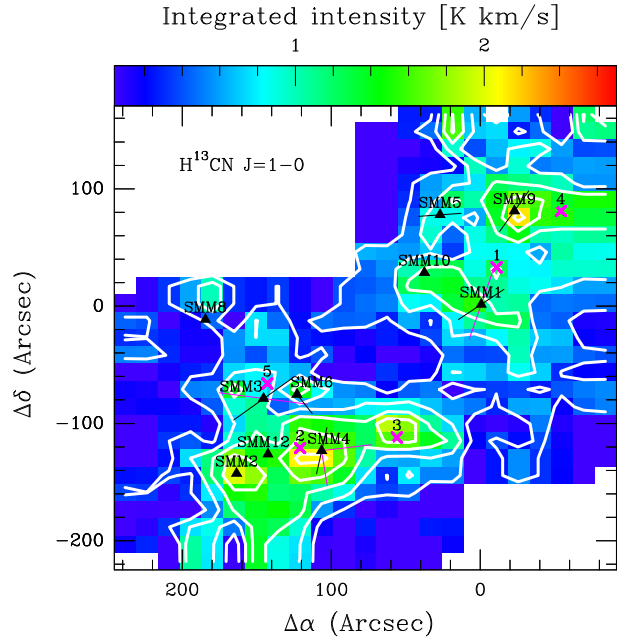


Fig. B.1: Similar to Fig. 2 but the emission of the  $\text{H}^{13}\text{CN } J = 1 - 0$  line. The first contour at  $10 \sigma$  level, with step of  $10 \sigma$



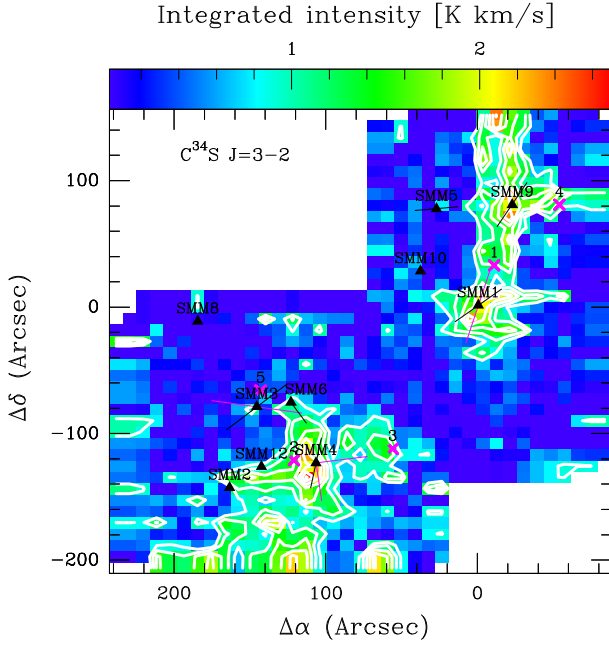


Fig. B.2: Similar to Fig. 2 but the emission of the  $C^{34}S$   $J = 3 - 2$  line. The first contour at  $30\sigma$  level, with step of  $10\sigma$

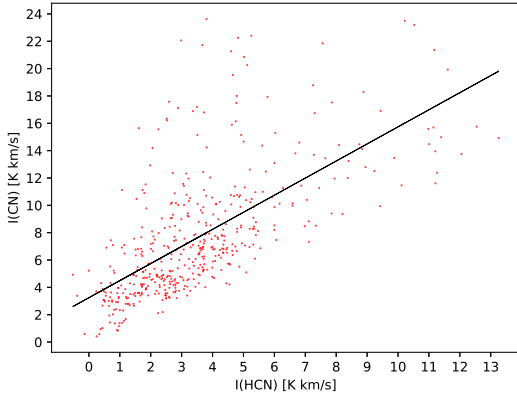


Fig. C.1: Correlation of CN  $J = 1 - 0$  and HCN  $J = 1 - 0$  integrated intensities  $\int T_{mb} dV$  for every pixel. A least-squares linear regression (black line) with following parameters: slope = 1.25, intercept = 0.24, stderr = 0.07. The Pearson correlation coefficient equals 0.65.

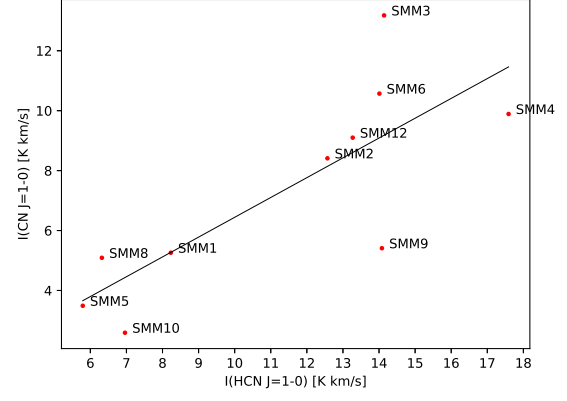


Fig. C.2: Correlation of CN  $J = 1 - 0$  and HCN  $J = 1 - 0$  integrated intensities  $\int T_{mb} dV$  for all sources. A least-squares linear regression (black line) with following parameters: slope = 0.66, intercept = -0.17, stderr = 0.18. The Pearson correlation coefficient equals 0.79.

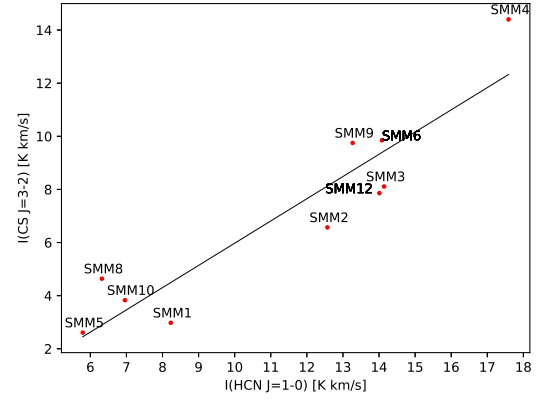


Fig. C.3: Similar to Fig. C.2 but CS  $J = 3 - 2$  and HCN  $J = 1 - 0$  lines correlation. A least-squares linear regression (black line) with following parameters: slope = 0.83, intercept = -2.39, stderr = 0.12. The Pearson correlation coefficient equals 0.93.

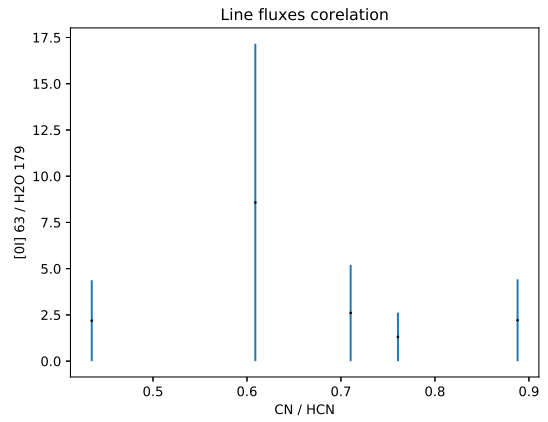


Fig. C.4: Correlation of [OI]  $63\mu m$  and  $H_2O$   $179\mu m$  fluxes.

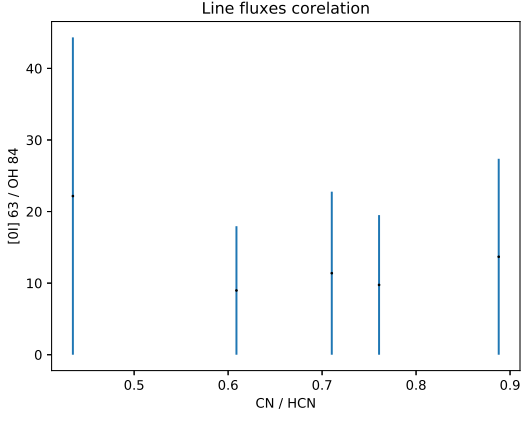


Fig. C.5: Correlation of [OI] 63  $\mu$ m and OH 84  $\mu$ m fluxes.

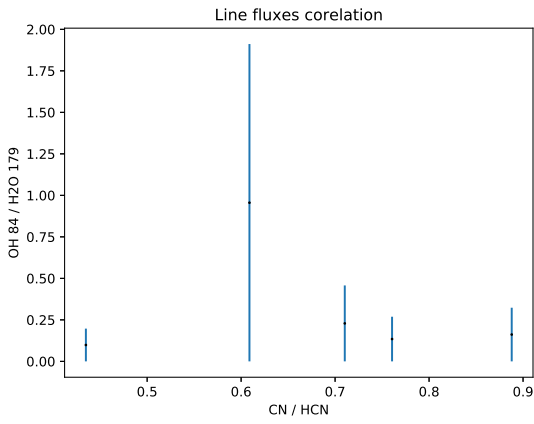


Fig. C.6: Correlation of OH 84  $\mu$ m and H<sub>2</sub>O 179  $\mu$ m fluxes.

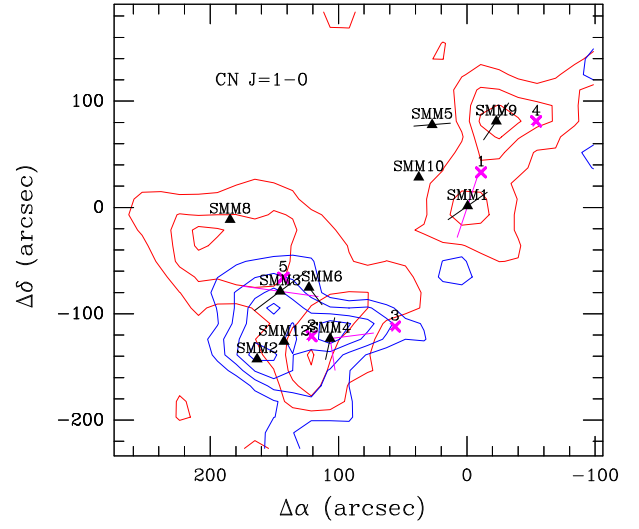


Fig. D.2: Similar to Fig. D.1 but the emission of the CN  $J=1-0$  line.

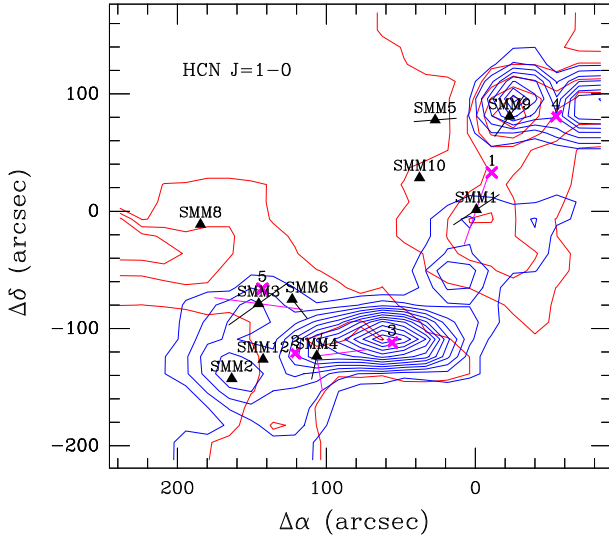


Fig. D.1: HCN  $J=1-0$  blue-shifted and red-shifted emission in Serpens Main region. The first contour is at  $5\sigma$  with the step of  $3\sigma$ . Triangles and lines marked as described in 2.